Magnetically tunable anti-plane wave bandgaps in 2D periodic two-phase hard-magnetic soft composites

Srikant Padmanabhan[1], Zeeshan Alam[1], Atul Kumar Sharma*

Soft Active Materials and Structures Laboratory, Department of Mechanical Engineering, Indian Institute of Technology Jodhpur 342037, India.

Abstract

The active manipulation of phononic bandgaps has been a topic of great interest in the recent past. Phononic crystals, or periodic composite structures built from soft elastomers, offer the potential for reversible manipulation of their phononic bandgaps through finite deformation of the periodic composite. By using hard-magnetic soft materials, which undergo reversible, finite deformations when subjected to an applied magnetic flux density, it is possible to tune the frequency ranges of elastic wave bandgaps or generate new bandgaps through magnetic stimuli. Here, we present a theoretical model for the analysis of large magneto-deformation and the anti-plane shear wave bandgaps in an infinite 2D periodic two-phase hard magnetic soft composite structure subjected to magnetic stimuli. The constitutive behavior of the phases in the hard-magnetic soft composite is described using the incompressible Gent model. To solve the incremental anti-plane wave equations, the finite element method and the Floquet-Bloch theorem for periodic medium are utilized. Using the developed framework, we numerically study the dependency of the bandgap width and their location on the direction and magnitude of applied magnetic flux density vector, material parameter contrasts, and geometry and volume fraction of the inclusion phase. The numerical results reveal that significant tunability of the bandgap is achieved when the applied magnetic flux density direction is along the residual magnetic flux density direction. Also, it is seen that the geometry of the inclusion has significant effect on the bandgap width.

Keywords: Phononic crystals, Wave propagation, Tunable band gaps, Soft materials, Hard-magnetic soft materials, Finite element method.

---

*Corresponding author

Email address: `atulksharma@iitj.ac.in` (Atul Kumar Sharma)

[1]Contributed equally

1. Introduction

Phononic Crystals (PnCs) have received growing attention since their discovery more than a decade ago. PnCs are engineered composite materials or structures designed to tailor the transmission of elastic waves, such as sound and vibrations, by creating periodic variations in the elastic properties of the constituent materials (Sigalas & Economou, 1992; Kim & Yang, 2014; Xia et al., 2019; Zhang & Gao, 2020; Vasileiadis et al., 2021; Chen et al., 2022; Liu et al., 2023). One of the key features of PnCs is the existence of band gaps (Kushwaha et al., 1993), which are frequency ranges where elastic/acoustic waves cannot propagate. The existence of band gaps in PnCs is attributed to Bragg scattering (Kushwaha et al., 1994) and local resonance (Raghavan & Phani, 2013). PnCs have a wide range of potential applications, including acoustic filters (Zhang & To, 2013), waveguides (Khelif et al., 2004), sensors (Gharibi & Mehaney, 2021), acoustic cloaking (Zheng et al., 2014), noise suppressors (Badreddine Assouar et al., 2012), multiplexing devices (Moradi & Bahrami, 2019), superlenses (Dubus et al., 2011) and many more.

One of the key challenges in design and development of PnCs is that the phononic bandgaps are typically fixed once the phononic composite/structure is manufactured. In contrast, there may be wide range of applications in which it is desirable to be able to actively tune the band gaps after the composite has been manufactured. To overcome this challenge of tunability, there have been several efforts in the recent past (Wang et al., 2008; Bou Matar et al., 2012; Nimmagadda & Matlack, 2019; Bertoldi & Boyce, 2008; Gei et al., 2011). In the context of PnCs made up of stiff/hard materials, tunability of band gaps has been explored using piezoelectrics (Wang et al., 2008, 2010; Vatanabe et al., 2014), magneo-elastics (Bou Matar et al., 2012; Hu et al., 2022), temperature variations Xia et al. (2016); Nimmagadda & Matlack (2019), etc, however, due to small-deformation of the structure tunability is limited. Recently, there has been growing interest in utilizing soft active materials, such as soft elastomers (Wang & Bertoldi, 2012; Bertoldi & Boyce, 2008; Rudykh & Boyce, 2014; Shim et al., 2015; Shmuel & Band, 2016; Chen et al., 2019), dielectric elastomers (Gei et al., 2011; Shmuel & deBotton, 2012; Shmuel, 2013; Getz et al., 2017; Jandron & Henann, 2018; Alam & Sharma, 2022; Zhao et al., 2023), and magneto-active elastomers (Pierce et al., 2020; Karami Mohammadi et al., 2019) which undergo large deformation when subjected to external stimuli to achieve significant tunability of phononic band gaps, i.e., shifting of band gaps.

In the present work, we consider phononic composites composed of hard-magnetic soft materials (HMSMs) that possess elastic wave band gaps. The size and location of these band gaps can be adjusted dynamically by applying an external magnetic flux density in real-time. HMSMs are a new family of soft magneto active materials that can undergo large, reversible deformations when actuated by magnetic field (Zhao et al., 2019; Moreno-Mateos et al., 2023; Rahmati et al., 2023b; Wang et al., 2020; Yan et al., 2023; Rahmati et al., 2023a). HMSMs differ from soft magneto-active elastomers in that they are manufactured by incorporating hard-magnetic particles with high-coercivity in the soft elastomer matrix (Lum et al., 2016; Kim et al., 2018; Wu et al., 2020a; Sano et al., 2022; Zhao & Zhang, 2022), while soft magneto active elastomers are manufactured by incorporating soft magnetic particles with low-coercivity in the elastomer matrix (Wu et al., 2020b; Garcia-Gonzalez et al., 2021). Further, HMSMs exhibit high remnant properties, allowing them to retain high residual magnetic flux density even when the external magnetic stimuli are removed. Owing to this property, significant efforts have gone into using HMSMs in a variety of engineering applications such as soft transducers (Lee et al., 2020; Nagal et al., 2022; Nandan et al., 2023), soft/flexible robotics (Kim et al., 2019; Wang et al., 2021), Metamaterials (Zhang et al., 2023), and many more. A recent review on the various applications of HMSMs may be found in Lucarini et al. (2022).

Using HMSMs as a route for obtaining magnetically tunable, soft PnCs was considered firstly by Zhang & Rudykh (2022) who developed a theoretical model for investigating the propagation of transverse elastic waves in 1D two-phase hard-magnetic soft laminates. They demonstrated the active manipulation of the band gaps in the shear mode with varying remanent magnetizations of the laminate constituents and found that a remotely applied magnetic field can significantly control the shear wave band gaps. Further, Alam et al. (2023) reported a 1D finite element model to investigate the longitudinal wave band gaps in hard-magnetic soft laminates. They demonstrated that the application of a magnetic flux density in the opposite direction to the residual magnetic flux density yields positive effects on the band gap properties of hard-magnetic soft laminates. In particular, increasing the applied magnetic flux density results in the widening of the band gap width and a shift towards higher frequencies. Li et al. (2022) investigated the active tuning of the band gaps in programmable hard-magnetic soft PnCs with three distinct magnetic anisotropy encoding modes through finite element simulation under the influence of an applied magnetic field. To the best of authors' knowledge, the propagation of elastic waves and tunable band gap characteristics of 2D two-phase hard-magnetic soft composites (HMSCs) has not been hitherto reported. To this end, we develop a numerical finite element framework for analyzing the propagation of incremental anti-plane waves superimposed on the magnetic field induced large deformation of the infinite 2D periodic two-phase HMSCs. Further, the developed numerical framework is utilized to demonstrate: (I) the magnetic tunability, (II) the influence of material parameter contrasts and volume fraction of composite phases, and (III) the influence of the geometry of the inclusion phase on the anti-plane wave band gap characteristics of the HMSC.

The remainder of manuscript is divided into five sections. Section 2 provides a concise overview of the fundamental formulation of the nonlinear field theory of HMSMs, along with its linearized incremental wave propagation theory. Section 3 presents a theoretical framework for analyzing the finite deformation behavior of a two-phase HMSC under a magnetic field in the quasi-static regime. In Section 4, we employ finite element method and Floquet-Bloch theorem to obtain the incremental anti-plane wave band gaps in an infinite 2D periodic two-phase HMSC. Section 5 presents the numerical results, which show how the applied external magnetic loading, volume fraction of phases, geometry of the inclusions, and material contrast parameters affect the band gap characteristics of an infinite 2D periodic HMSC. Finally, in Section 6, we summarize the conclusions drawn from the current study and also provide further outlook.

2. Dynamics of hard-magnetic soft composites

In this section, we provide a concise review of the governing equations pertaining to the dynamics of deformable HMSCs following the the nonlinear field theory of HMSMs (Zhao et al., 2019) and the related linearized incremental theory (Dorfmann & Ogden, 2014).

Consider an arbitrary incompressible, soft, deformable, hard-magnetic, soft-composite body made up of two phases a and b. This body occupies a domain $\Omega_R^a \cup \Omega_R^b = \Omega_R \subset \mathbb{R}^3$ with the boundary $\partial\Omega_R$ in the reference configuration. When actuated by biasing magnetic fields, the composite body undergoes deformation and occupies a domain $\Omega^a \cup \Omega^b = \Omega \subset \mathbb{R}^3$ in the current configuration. The boundary of the body in the current configuration is labeled by $\partial\Omega$. The deformation $\boldsymbol{\chi} : \Omega_R \to \Omega$ maps material particles $\mathbf{X}$ in the reference configuration to the spatial points $\mathbf{x}$ in the current configuration. In the following discussion, the differential operators 'Grad', 'Div', and 'Curl' are used to denote the gradient, divergence, and curl in the reference configuration, respectively, while 'grad', 'div', and 'curl' are used to denote the same operators in the current configuration. For defining different relevant fields in the current and reference configurations, we introduce the deformation gradient tensor $\mathbf{F}$, Jacobian J, and the left Cauchy-Green strain tensor $\mathbf{b}$.

$$\mathbf{F} = \mathrm{Grad}\boldsymbol{\chi}, \qquad J = \det \mathbf{F} > 0, \qquad \mathbf{b} = \mathbf{F}\mathbf{F}^{\mathrm{T}}. \tag{1}$$

Neglecting the mechanical body forces, the *total* Cauchy stress tensor σ satisfies the balance of linear momentum equation in the current configuration as follows:

$$\mathrm{div}\boldsymbol{\sigma} = \rho\mathbf{a} \tag{2}$$

where ρ denotes the material mass density, which remains constant as the material is incompressible $J = 1$, and $\mathbf{a} = \boldsymbol{\chi}_{,tt}$ represents the acceleration.

In the case of an ideal hard-magnetic soft material (with no free current) and neglecting the dynamic coupling between electro-magnetic fields, the Maxwell equations in the current configuration can be expressed as follows

$$\mathrm{div}\mathbf{B} = 0, \qquad \mathrm{curl}\mathbf{H} = \mathbf{0} \tag{3}$$

here, $\mathbf{H}$ and $\mathbf{B}$ are the magnetic field and the magnetic flux density in the current configuration, respectively.

Jump boundary conditions between interfaces separating phases a and b are:

$$[\![\boldsymbol{\sigma}]\!] \cdot \mathbf{n} = \mathbf{0}, \qquad \mathbf{n} \cdot [\![\mathbf{B}]\!] = 0, \qquad \mathbf{n} \times [\![\mathbf{H}]\!] = \mathbf{0} \tag{4}$$

here, $[\![\bullet]\!] = (\bullet)^a - (\bullet)^b$ represents the jump operator, and $\mathbf{n}$ denotes the unit normal vector to the surface element in the deformed configuration.

The constitutive relations for an incompressible hyperelastic hard-magnetic material are obtained from the nominal Helmholtz free energy density function $\Psi(\mathbf{F}, \mathbf{B}_0)$ (per unit volume in the undeformed configuration) (Zhao et al., 2019) as follows:

$$\mathbf{P}=\frac{\partial\Psi}{\partial\mathbf{F}}+\gamma\mathbf{F}^{-\mathbf{T}},\qquad \mathbf{H}_0=\frac{\partial\Psi}{\partial\mathbf{B}_0} \tag{5}$$

where $\mathbf{P}=J\boldsymbol{\sigma}\mathbf{F}^{-\mathrm{T}}$, $\mathbf{H}_0=\mathbf{F}^{\mathrm{T}}\mathbf{H}$, and $\mathbf{B}_0=J\mathbf{F}^{-1}\mathbf{B}$ are the *totol* first Piola-Kirchhoff stress tensor, Lagrangian magnetic field and magnetic flux density vectors, respectively, and γ is an arbitrary scalar accounting for the incompressibility constraint.

Following Dorfmann & Ogden (2014), we consider a time-dependent small amplitude incremental wave motion $\dot{\mathbf{x}}=\dot{\boldsymbol{\chi}}(\mathbf{X},t)$, along with an incremental change $\dot{\mathbf{B}}_0(\mathbf{X},t)$ in magnetic flux density, superimposed on the quasi-static large magnetodeformation of the hard magnetic soft body $\Omega(\boldsymbol{\chi})$. In the sequel, to distinguish the incremental quantities from their equilibrium counterparts, we use a dot above them.

In the updated Lagrangian form, the governing equations for the incremental motion and magnetic field are written as:

$$\mathrm{div}\boldsymbol{\Sigma}=\rho\dot{\mathbf{x}}_{,tt},\qquad \mathrm{div}\check{\mathbf{B}}=0,\qquad \mathrm{curl}\check{\mathbf{H}}=\mathbf{0} \tag{6}$$

where $\boldsymbol{\Sigma}=J^{-1}\dot{\mathbf{P}}\mathbf{F}^{\mathrm{T}}$, $\check{\mathbf{B}}=J^{-1}\mathbf{F}\dot{\mathbf{B}}_0$, and $\check{\mathbf{H}}=\mathbf{F}^{-\mathrm{T}}\dot{\mathbf{H}}_0$ are the *push-forwards* of increments in Lagrangian quantities $\dot{\mathbf{P}}$, $\dot{\mathbf{B}}_0$, and $\dot{\mathbf{H}}_0$, respectively.

For an incompressible hard-magnetic soft material, the linearized incremental constitutive equations are written as

$$\boldsymbol{\Sigma}=\mathscr{C}\mathbf{h}-\gamma\mathbf{h}^{\mathrm{T}}+\dot{\gamma}\mathbf{I}+\mathscr{B}\check{\mathbf{B}},\qquad \check{\mathbf{H}}=\mathscr{B}^{\mathrm{T}}\mathbf{h}+\mathscr{A}\check{\mathbf{B}}, \tag{7}$$

where $\mathscr{C}$, $\mathscr{B}$, and $\mathscr{A}$ are the constitutive tensors and their components are written as

$$\mathscr{C}_{ijkl}=\frac{1}{J}F_{jI}\frac{\partial^2\Psi}{\partial F_{iI}\partial F_{kJ}}F_{lJ},\quad \mathscr{B}_{ijk}=F_{jI}\frac{\partial^2\Psi}{\partial F_{iI}\partial B_{0J}}F^{-1}_{Jk},\quad \mathscr{A}_{ij}=JF^{-1}_{Ii}\frac{\partial^2\Psi}{\partial B_{0I}\partial B_{0J}}F^{-1}_{Jj} \tag{8}$$

and $\dot{\gamma}$ is the increment in γ, and the incremental displacement gradient tensor $\mathbf{h}=\mathrm{grad}\dot{\mathbf{x}}$ satisfies the material incompressibility constraint $\mathrm{tr}\mathbf{h}=\mathrm{div}\dot{\mathbf{x}}=0$.

3. Nonlinear Magnetodeformation of two-phase hard-magnetic soft composites

We consider a 2-D periodic two-phase composite consisting of square-shaped inclusions (incompressible hard-magnetic soft phase a) and embedded in a different incompressible hard-magnetic soft material (phase b) which is infinitely large in the (x_1, x_3) plane. The composite is infinitely long along x_2 direction and the different magneto-mechanical fields are assumed to be invariant with respect to x_2 direction. In the undeformed configuration, the unit cell for this 2-D periodic two-phase composite is assumed to be a square of length L as shown in Fig. 1(a). Hereafter, the superscript $(\bullet)^p$ is used to denote the physical quantities of the composite phases $(p = a, b)$.

To describe the constitutive response of the HMSC, we consider that the hard-magnetic soft phases are modeled by the incompressible Gent model of hyperelasticity (Gent, 1996) in conjunction with the ideal hard-magnetic soft material model (Zhao et al., 2019). The expression for the Helmholtz free energy of the ideal hard-magnetic soft phase is given by

$$\Psi^p = -\frac{G^p J^p_{\mathrm{lim}}}{2} \ln\left[1 - \frac{\mathrm{tr}\,\mathbf{b}^p - 3}{J^p_{\mathrm{lim}}}\right] - \frac{1}{\mu_0}\mathbf{F}^p\mathbf{B}^p_{r_0} \cdot \mathbf{B}^{\mathrm{applied}^p} \tag{9}$$

where G^p is the shear modulus, J^p_{lim} is the limiting stretch parameter, μ_0 is the vacuum permeability, $\mathbf{B}^p_{r_0}$ is the residual magnetic flux density vector in the reference configuration, and $\mathbf{B}^{\mathrm{applied}^p}$ is the applied magnetic flux density vector in the current configuration. Utilizing Eqs. (5) (9), the total Cauchy stress generated in each phase is obtained as

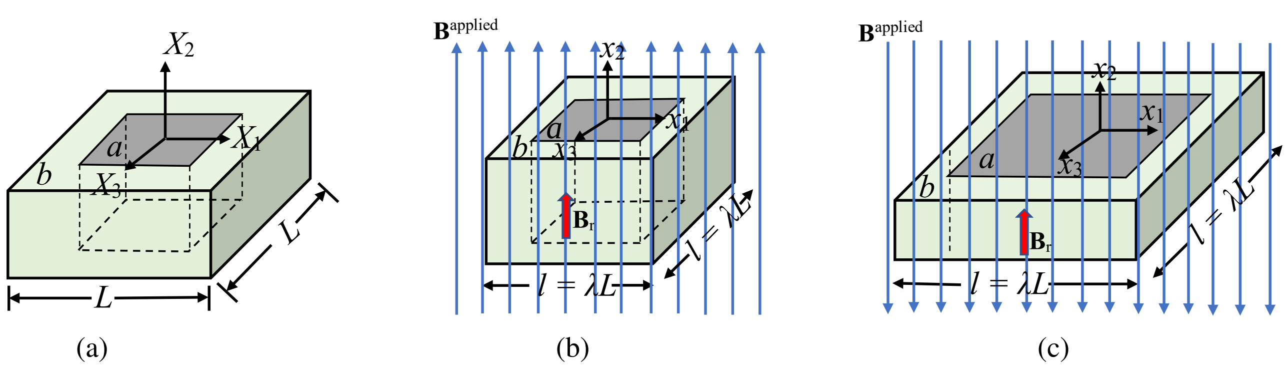

Figure 1: Schematic description of a two-phase HMSC with square shape inclusion in (a) reference configuration, (b) current configuration with residual magnetic flux density aligned with the direction of applied magnetic flux density, and (c) current configuration with residual magnetic flux density opposing the direction of applied magnetic flux density.

$$\boldsymbol{\sigma}^p = \frac{G^p}{\left[1 - \dfrac{\mathrm{tr}\,\mathbf{b}^p\ -\ 3}{J^p_{\mathrm{lim}}}\right]}\mathbf{b}^p - \frac{1}{\mu_0}\mathbf{B}^{\mathrm{applied}^p} \otimes \mathbf{F}^p\mathbf{B}^p_{r_0} + \gamma^p\mathbf{I}. \tag{10}$$

For known values of residual and applied magnetic flux density vectors, respectively, the total Cauchy stress tensor $\boldsymbol{\sigma}^p$ is a function of the deformation gradient tensor $\mathbf{F}$ only. Further, if in the current configuration, the direction of $\mathbf{B}^{\mathrm{applied}^p}$ is parallel to the direction of $\mathbf{B}^p_{r_0}$, the total Cauchy stress becomes symmetric. However, for more general cases, the total Cauchy stress tensor is asymmetric Zhao et al. (2019); Zhang et al. (2023).

We consider that the composite phases are perfectly bonded and is subjected to the magnetic magnetic flux density in the x_2 direction (parallel to the direction of residual magnetic flux density vector) only, as shown in Fig. 1. The presence of perfect bonding between phases leads to homogeneous deformation and magnetic flux density in each phase, which can be described as

$$\mathbf{F}^p = \begin{bmatrix} \lambda & 0 & 0 \\ 0 & \lambda^{-2} & 0 \\ 0 & 0 & \lambda \end{bmatrix}, \qquad \mathbf{B}^{\mathrm{applied}^p} = \begin{bmatrix} 0 \\ B_2 \\ 0 \end{bmatrix} \tag{11}$$

where λ denotes the in-plane stretch ratio and B_2 is the component of the magnetic flux density vector along x_2 direction. Substituting Eq. (11) into Eq. (10), the expressions for the the nonzero components of total Cauchy stress tensor in terms B_2 and λ are obtained as

$$\sigma^p_{11} = \sigma^p_{33} = \frac{G^p\lambda^2}{\left[1 - \dfrac{2\lambda^2 + \lambda^{-4} - 3}{J^p_{\mathrm{lim}}}\right]} + \gamma^p, \quad \sigma^p_{22} = \frac{G^p\lambda^{-4}}{\left[1 - \dfrac{2\lambda^2 + \lambda^{-4} - 3}{J^p_{\mathrm{lim}}}\right]} + \gamma^p - \frac{B_2 B^p_{r_{0_2}}}{\mu_0\lambda^2}, \tag{12}$$

where $B^p_{r_{0_2}}$ is the component of residual magnetic flux density vector for p^{th} phase.

For fulfilling the traction free boundary conditions, the components of total Cauchy stress tensors must satisfy

$$\sigma^p_{11} = \sigma^p_{33} = 0, \qquad \nu^a\sigma^a_{22} + \nu^b\sigma^b_{22} = 0 \tag{13}$$

where ν^a and $\nu^b = 1 - \nu^a$ are the volume fractions of the phases a, and b, respectively. Utilizing the Eqs 13 and 12 and assuming limiting stretch parameter $J^a_{\text{lim}} = J^b_{\text{lim}} = J_{\text{lim}}$, we obtain the nonlinear relationship between the applied magnetic flux density B_2, and the in-plane stretch ratio λ as

$$\frac{\lambda^{-2} - \lambda^4}{\left[1 - \dfrac{2\lambda^2 + \lambda^{-4} - 3}{J_{\text{lim}}}\right]} = \frac{\bar{B}_{r0_2} B_2}{\bar{G}\mu_0}, \tag{14}$$

where $\bar{G} = G^a\nu^a + G^b\nu^b$, and $\bar{B}_{r0_2} = B^a_{r0_2}\nu^a + B^b_{r0_2}\nu^b$.

According to Eq. (14), the in-plane stretch ratio λ can be found once the material parameters and the applied magnetic flux density B_2 are prescribed.

4. Incremental anti-plane waves in a 2D infinite periodic two-phase hard-magnetic soft composite

Based on the magnetically induced nonlinear finite deformation obtained in the aforementioned section, we now study the superimposed incremental anti-plane elastic shear waves propagating in the plane (x_1, x_2) of the HMSC. We assume that the anti-plane strain condition holds ($\dot{x}_1 = \dot{x}_3 = 0$) and the incremental anti-plane displacement field $\dot{x}_2$ depends on coordinates (x_1, x_3) and time t. For propagation of anti-plane shear waves in HMSC, the governing incremental equation of motion (Eq. 6) takes the following form

$$\frac{\partial \Sigma_{21}(x_1, x_3, t)}{\partial x_1} + \frac{\partial \Sigma_{23}(x_1, x_3, t)}{\partial x_3} = \rho(x_1, x_3)\frac{\partial^2 \dot{x}_2(x_1, x_3, t)}{\partial t^2}. \tag{15}$$

Using incompressibility constraint ($h_{22} = 0$) and incremental constitutive relation (Eq. 7), the components Σ_{21} and Σ_{23} are obtained as

$$\Sigma_{21} = \mathscr{C}_{2121} h_{21} + \mathscr{C}_{2123} h_{23}, \quad \Sigma_{23} = \mathscr{C}_{2323} h_{23} + \mathscr{C}_{2321} h_{21} \tag{16}$$

where, $\mathscr{C}_{2121} = \mathscr{C}_{2323} = G(x_1, x_3)\dfrac{\lambda^2}{\left[1 - \dfrac{2\lambda^2 + \lambda^{-4} - 3}{J_{\text{lim}}}\right]} = \tilde{G}$ and $\mathscr{C}_{2123} = \mathscr{C}_{2321} = 0$.

Assuming incremental anti-plane displacement field to be time-harmonic as $\dot{x}_2(x_1, x_3, t) = u_2(x_1, x_3)\exp(-i\omega t)$, and inserting the components Σ_{21} and Σ_{23} from Eq. (16) into Eq. (15), we obtain the incremental anti-plane wave equation in the frequency domain as

$$\frac{\partial}{\partial x_1}\left(\tilde{G}\frac{\partial u_2(x_1,x_3)}{\partial x_1}\right)+\frac{\partial}{\partial x_3}\left(\tilde{G}\frac{\partial u_2(x_1,x_3)}{\partial x_3}\right)=-\omega^2\rho(x_1,x_3)u_2(x_1,x_3) \tag{17}$$

where $u_2(x_1, x_3)$ is the incremental anti-plane displacement field that is spatially dependent, and ω is the angular frequency associated with the anti-plane wave motion.

Next, we employ standard displacement based finite element approach to solve Eq. (17). The weak form of Eq. (17) is obtained by multiplying it with test function δw, and then integrating over the entire computational domain (2D HMSC unit cell depicted in Fig. 2a) as

$$\int_{\Omega_t}\tilde{G}\left(\frac{\partial u_2}{\partial x_1}\frac{\partial \delta w}{\partial x_1}+\frac{\partial u_2}{\partial x_3}\frac{\partial \delta w}{\partial x_3}\right)dx_1dx_3=\int_{\Omega_t}\omega^2\rho u_2\delta w dx_1dx_3. \tag{18}$$

The computational domain is divided into a set of 4-noded quadrilateral element finite elements $\Omega_t = \bigcup_{e=1}^{nel}\Omega_t^e$, and the incremental displacement field u_2 and test function δw are interpolated element-wise in terms of nodal quantities using nodal shape functions as

$$u_2 = N^I u_2^I, \quad \delta w = N^I \delta w^I, \tag{19}$$

where N^I represents the nodal shape function with I denoting the number of nodes in a finite

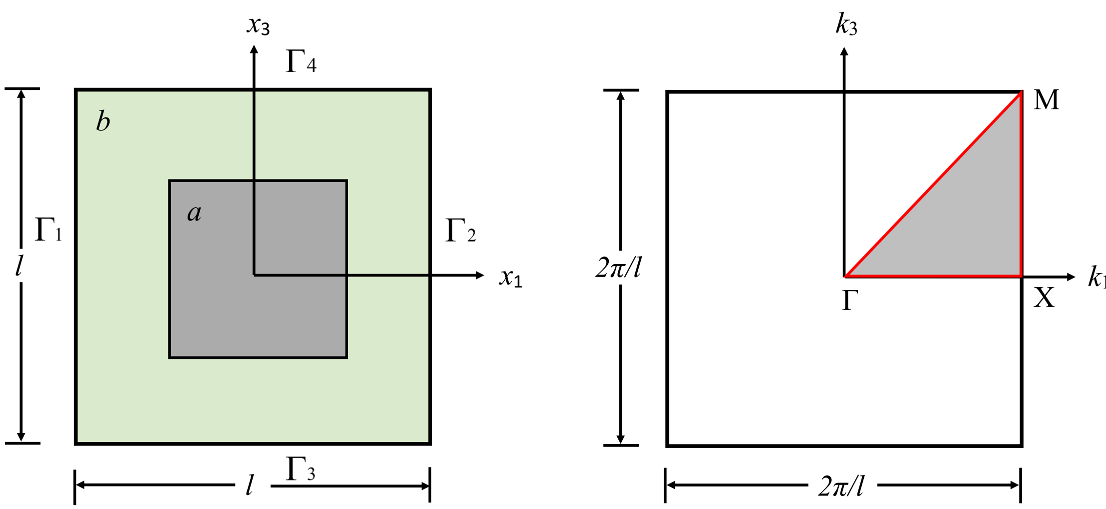

(a) (b)

Figure 2: Schematic of the deformed unit cell in the plane of periodicity (x_1, x_3), and (b) the corresponding first Brillouin zone.

element, and u_2^I is the incremental anti-plane displacement values at node I. Upon substituting the finite approximations from Eq. (19) into Eq. (18), we obtain the eigenvalue problem as

$$\bigcup_{e=1}^{nel} \mathbf{K}^e u_2^J = \omega^2 \bigcup_{e=1}^{nel} \mathbf{M}^e u_2^J \tag{20}$$

where

$$\mathbf{K}_{IJ}^e = \int_{\Omega_t^e} \tilde{G} \frac{\partial N^I}{\partial x_j} \frac{\partial N^J}{\partial x_j} dx_1 dx_3, \quad \mathbf{M}_{IJ}^e = \int_{\Omega_t^e} \rho N^I N^J dx_1 dx_3, \tag{21}$$

are the components of elemental level stiffness $\mathbf{K}^e$ and mass $\mathbf{M}^e$ matrices, respectively, and index $j = 1,\ 3$.

Next, we employ Bloch-Floquet theorem (Kittel et al., 1996) for obtaining the anti-plane wave band structure of an infinite periodic two-phase HMSC. According to Bloch-Floquet theorem, the incremental anti-plane displacement field must satisfy

$$u_2\left(x_{\Gamma_2}\right) = \exp(ik_1 l) u_2\left(x_{\Gamma_1}\right), \quad u_2\left(x_{\Gamma_4}\right) = \exp(ik_3 l) u_2\left(x_{\Gamma_3}\right), \tag{22}$$

in which k_1 and k_3 denote the components of 2D Bloch wave vector $\boldsymbol{k} = k_1\mathbf{e}_1 + k_2\mathbf{e}_2$, varying along the edges $[\Gamma - \mathrm{X} - \mathrm{M} - \Gamma]$ of the deformed first irreducible Brillouin zone for the square unit cell (Wang et al., 2007) as depicted in Fig. 2b and Γ_1, Γ_2, Γ_3, and Γ_4 are the boundaries of the unit cell as shown in Fig. 2a. We implemented the Bloch-Floquet complex-valued boundary conditions (Eq. 22) using augmented penalty method (Alam et al., 2023; Felippa, 2001). By solving the eigenvalue problem (Eq. 20) in conjunction with the complex-valued boundary conditions (Eq. 22), we obtain the band structure. The aforementioned numerical framework of extracting the anti-plane wave band structure is implemented through a MATLAB code developed in-house.

5. Numerical results and discussion

In this section, we present the numerical results to investigate the effect of applied magnetic loading, inclusion geometry and volume fraction (Phase b), and material parameter contrasts on the tunability of the elastic anti-plane shear wave bandgap structure of the two-phase HMSC.

In the numerical simulations, we discretize the undeformed unit cell, with geometric parameter

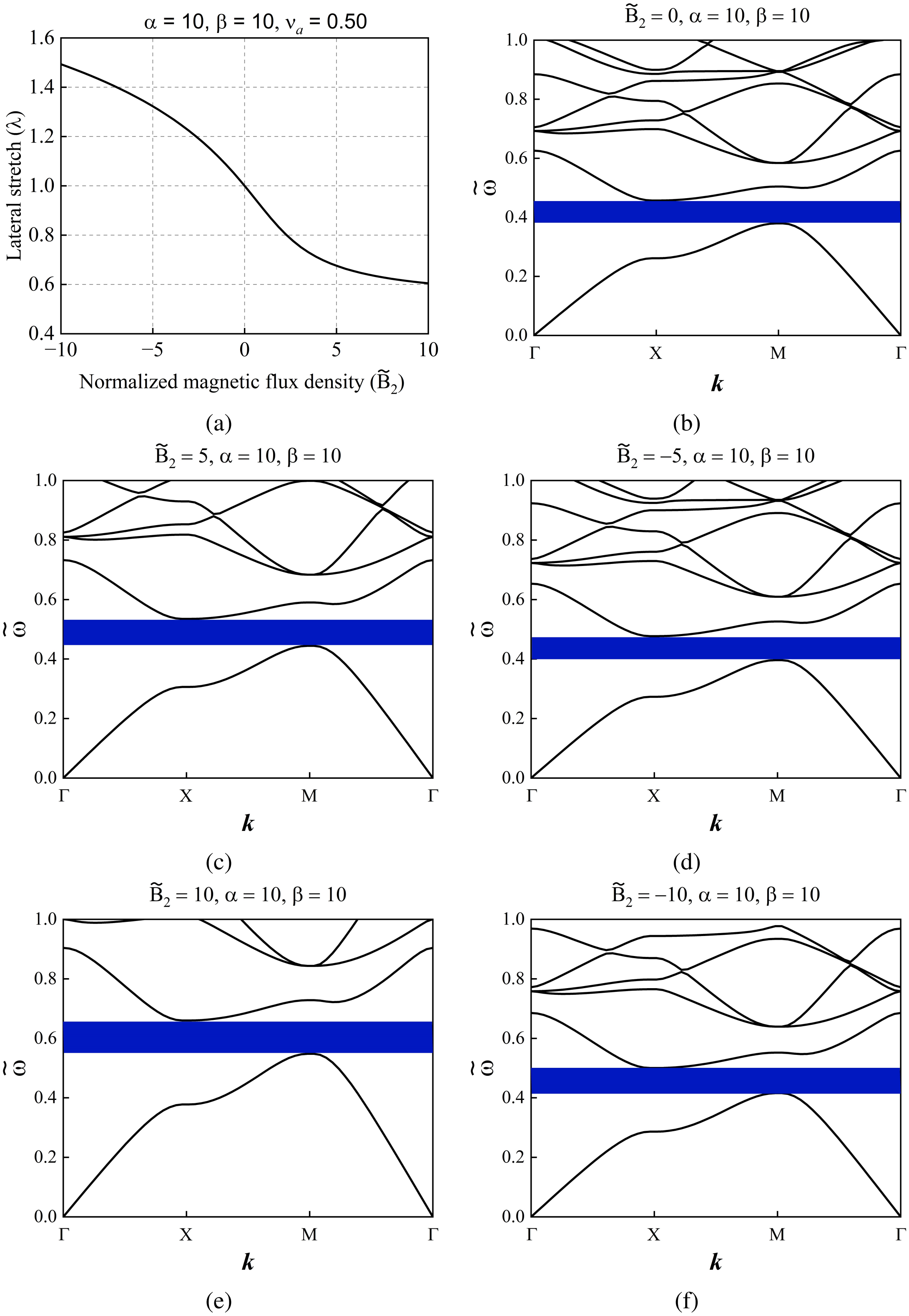

Figure 3: (a) Nonlinear finite mgnetodeformation response of the composite. (b-f) Band structures of the two-phase HMSC subjected to the different levels of normalized applied magnetic flux density. The normalized frequencies $\tilde{\omega}$ are plotted as functions of the reduced wave vector $\boldsymbol{k}$ along $\Gamma - \mathrm{X} - M - \Gamma$.

$L = 5$ mm, using 4-noded quadrilateral elements with a single degree of freedom, i.e., the anti-plane displacement field. We examine a HMSC with Phase b possessing the following material properties: b: $G^b = 303$ kPa, $\rho^b = 2434$ kg/m^3, $Br0_2{}^b = 0.143$ T, and extract the band structure for representative values of phase a material properties defined using the shear contrast parameter $\alpha = \frac{G^a}{G^b}$, magnetic contrast parameter $\beta = \frac{B^a_{r_{0_2}}}{B^b_{r_{0_2}}}$, and volume fraction $\nu_a = 1 - \nu_b$ at different values of the normalized applied magnetic flux density, denoted as $\tilde{B}_2 = \frac{B_2}{\sqrt{(\nu^a G^a + \nu^b G^b)\,\mu_0}}$. We assume that the mass density of phase a is the same as that of Phase b, i.e., $\rho^b = 2434$ kg/m^3. We take the limiting stretch parameter to be $J_{\rm lim} = 10$. Note that in the initial numerical results presented herein to investigate the influence of external magnetic loading, volume fraction of the inclusion, and material parameter contrasts on the bandgap characteristics, we consider an inclusion with a square cross-section as shown in Fig. 2a. Later, we investigate the effect of inclusions with three different geometries on the bandgap characteristics while keeping other material parameters constant.

5.1. Quasi-static finite deformation and magnetic tunability of the phononic band gaps

Here, we analyze the quasi-static nonlinear large magnetodeformation and tunability of the superimposed incremental anti-plane wave band gap characteristics of the HMSC at different levels of normalized applied magnetic flux density. The nonlinear algebraic equation Eq. (14) is solved to analyze the quasi-static nonlinear finite deformation. Figure 3(a) demonstrates the variation of the stretch parameter λ as a function of the normalized magnetic flux density $\tilde{B}_2$ for a HMSC with $\alpha = 10$, $\beta = 10$, and $\nu^a = 0.5$. When the magnetic flux density is applied in the same direction as the residual magnetic flux density, denoted by ($\tilde{B}_2 > 0$), the HMSC undergoes expansion along the

Table 1: Variation of the normalized bandgap width ($\Delta\tilde{\omega}_1$) and the frequency range ($\tilde{\omega}_{1_{\max}} - \tilde{\omega}_{2_{\min}}$) of the first anti-plane wave bandgap with normalized applied magnetic flux density ($\tilde{B}_2$).

$\tilde{B}_2 \rightarrow$	-10	-5	0	5	10
$\Delta\tilde{\omega}_1$	0.0848	0.0809	0.0775	0.0907	0.1119
$\tilde{\omega}_{1_{\max}} - \tilde{\omega}_{2_{\min}}$	0.4156 - 0.5004	0.3962 - 0.4771	0.3795 - 0.4570	0.4443 - 0.5350	0.5482 - 0.6601

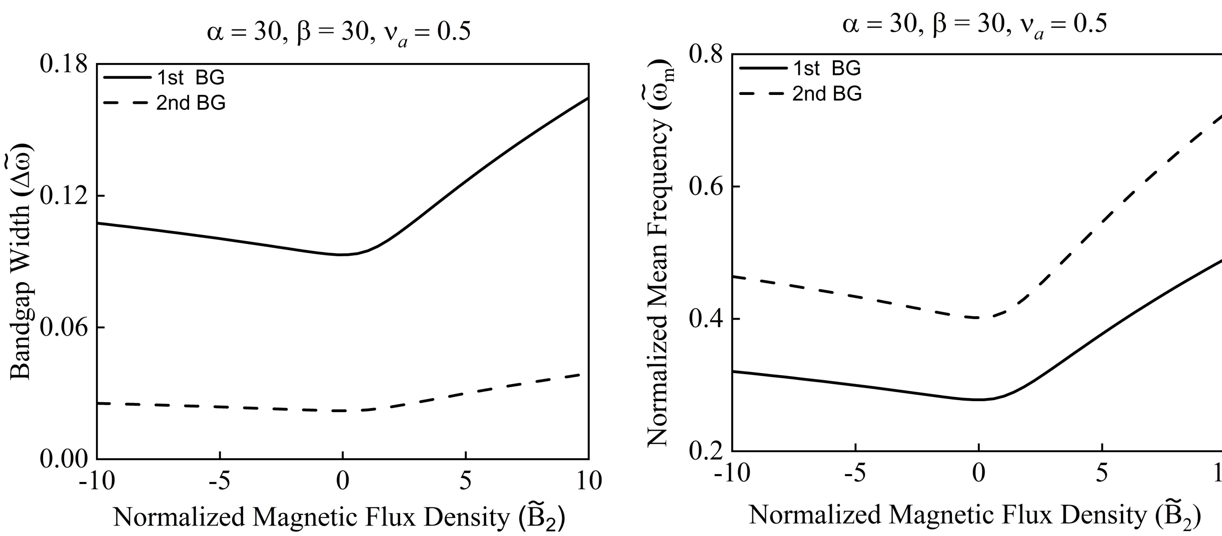

(a) (b)

Figure 4: Variation of the first and second band gap (a) widths, and (b) mean of the frequency limits as a function of normalized applied magnetic flux density $\tilde{\mathrm{B}}_2$.

x_2 direction ($\lambda < 1$). Conversely, when the magnetic flux density is applied in the opposite direction of the residual magnetic flux density, indicated by ($\tilde{B}_2 < 0$), the composite contracts in the x_2 direction ($\lambda > 1$) due to the compressive magnetic stress. Furthermore, to explore the dependence of the band gap characteristics on the applied magnetic flux density, we consider five different cases: (I) $\tilde{B}_2 = 0$, (II) $\tilde{B}_2 = -5,\ -10$, and (III) $\tilde{B}_2 = 5,\ 10$. Figures 3(b-f) display the band gaps along the boundaries of the irreducible first Brillouin zone for the composite when subjected to the aforementioned five levels of magnetic flux density $(\tilde{B}_2)$, where $\tilde{\omega} = \dfrac{\omega L}{2\pi}\sqrt{\dfrac{\rho}{\nu^a G^a + \nu^b G^b}}$ is the normalized frequency of the anti-plane wave. The band gap width in the band structure plots is depicted by blue regions. The values of the stretch parameter λ corresponding to the above-mentioned values of $\tilde{B}_2$ are 1, 1.3227, 1.4934, 0.6759, and 0.6047, respectively. The width and corresponding normalized frequency ranges of the first bandgap for the aforementioned applied levels of normalized magnetic flux density $\tilde{B}_2$ are listed in Table 1. It is observed from Fig. 3(b-f) and Table 1 that the band gap size increases with an increase in the magnitude of applied magnetic flux density in both cases, i.e., Case II: when the direction of applied magnetic flux density is along the direction of residual magnetic flux density, and Case III: when the direction of applied magnetic flux density is opposite to the direction of residual magnetic flux density. It is also observed that the location of the band gap shifts towards a higher frequency range in both cases. Figure 4 (a) illustrates the variation of the width of the first and second bandgaps as a function of the normalized magnetic flux density $\tilde{B}_2$, while Fig. 4 (b) illustrates the variation of the mean of the normalized band gap frequency limits $\tilde{\omega}_m$. From Fig. 4, it is clearly seen that the rate of increase in the width and mean of the frequency limits of band gaps is higher in the case of applied magnetic flux density along the direction of residual magnetic flux density ($\tilde{B}_2 > 0$). By magnetically actuating the HMSC, the width of the first bandgap is increased by 44.38% when the applied magnetic flux density is $\tilde{B}_2 = 10$ and by 9.42% when the applied magnetic flux density is $\tilde{B}_2 = -10$. This observation shows that applying magnetic loading in the direction of the residual magnetic flux density has a positive influence on the tunability of band gaps.

5.2. Parametric study of material parameter contrasts and volume fraction of phases

Firstly, we will investigate how the variation in the shear contrast parameter α affects the bandgap characteristics of a two-phase HMSC. The shear contrast significantly affects the width and location of the bandgaps. Figure 5 (a-c) displays the normalized frequency ω as a function of the wave vector **k** for a magnetically actuated two-phase HMSC with three distinct values of shear contrast α = 10, 20, and 30, respectively. In the numerical simulations for these three cases, we keep other parameters constant, such as $\beta = 30$, $\tilde{B}_2 = 10$, and $\nu_a = 0.5$. The variation of the bandgap widths of the first and second bandgaps with the shear contrast α is depicted in Fig. 6 (a). Figure 6 (b) illustrates the variation of the mean of the normalized frequency limits, $\tilde{\omega}_m$, as a function of the shear contrast α. From Fig. 6 (a), we observe that the first bandgap opens at $\alpha = 4.5$, and the width of the bandgap increases with shear contrast α, reaching a maximum at $\alpha = 15$, and then decreasing. On the other hand, it is worth noting that the second bandgap opens at higher values of shear contrast $\alpha = 16$, and the width of the second bandgap increases with an increase in α. From Fig. 6 (b), we can see that the location of both bandgaps shifts towards the lower frequency range. These inferences can be utilized in the design of wave-manipulating devices with applications in the lower frequency range.

Next, we examine the impact of the magnetic contrast parameter β on the bandgap characteristics of the two-phase HMSC with square inclusions. Figure 7 illustrates the band structures of the composite for three different values of the magnetic contrast parameter: β = 10, 20, and 30. In the numerical simulations, we take volume fraction $\nu_a = 0.5$, shear contrast $\alpha = 30$, and normalized magnetic flux density $\tilde{B}_2 = 10$. Figure 8(a) shows the variation of the widths of the first and second

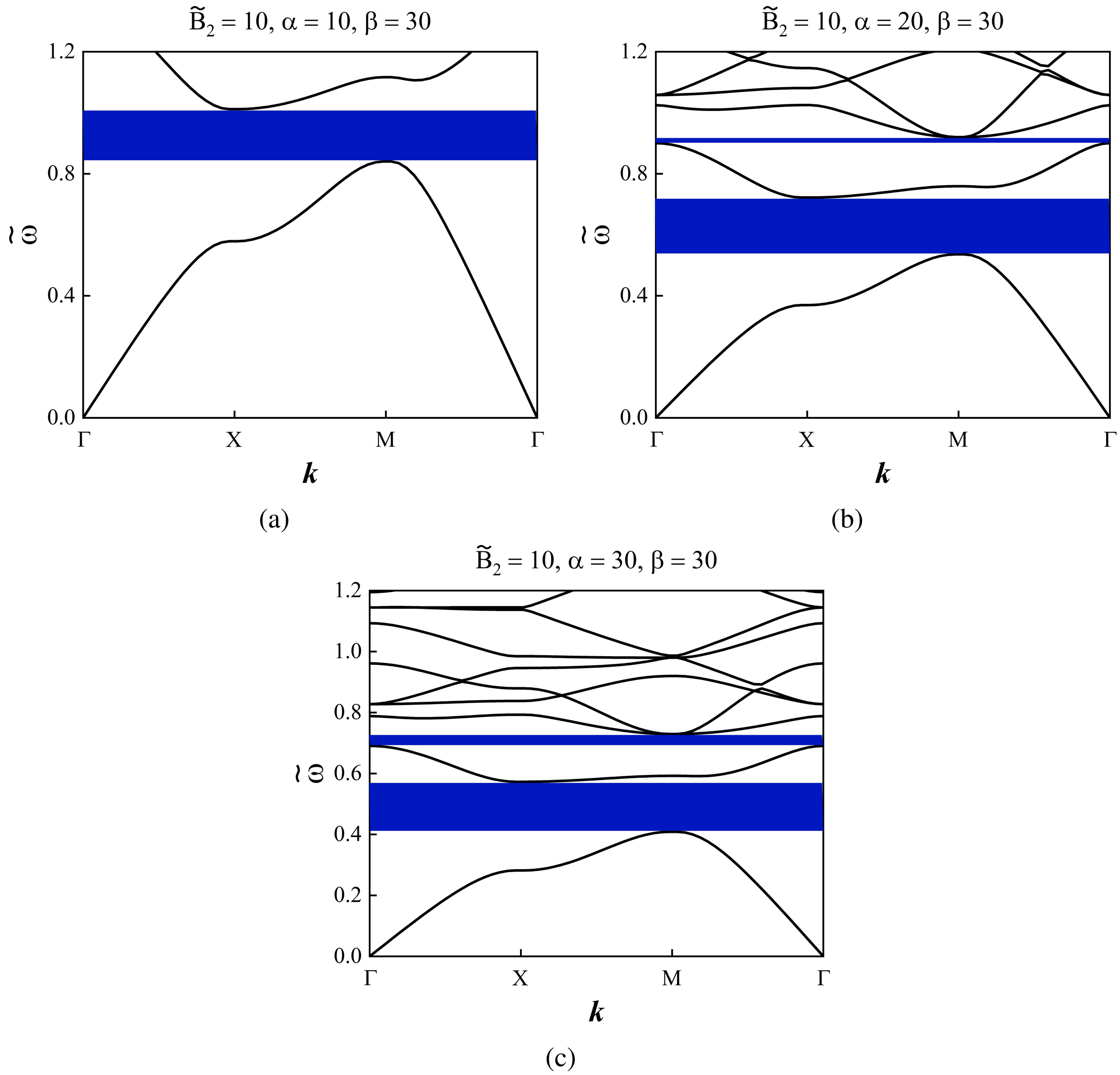

Figure 5: Band structures of the two-phase HMSC at different values of shear contrast parameter α, while keeping the magnetic contrast parameter β, and the normalized magnetic flux density $\tilde{B}_2$ as constant.

bandgaps with the magnetic contrast parameter β, while Fig. 8 (b) illustrates the variation of mean of the normalized frequency limits $\tilde{\omega}$. Figures 7 and 8 reveal that the widths and the location of the band gaps increases with an increase in the magnetic parameter contrast. However, the effect of β on band gap tunability is much more modest than that of α for the contrast values considered in the present study.

The tunability of bandgaps in HMSC is strongly influenced by the volume fraction of the inclusion ν_a. In order to extract the influence of volume fraction on the band gap characteristics, We varies the volume fraction of inclusion from from 0 to 1, while other material parameters are kept

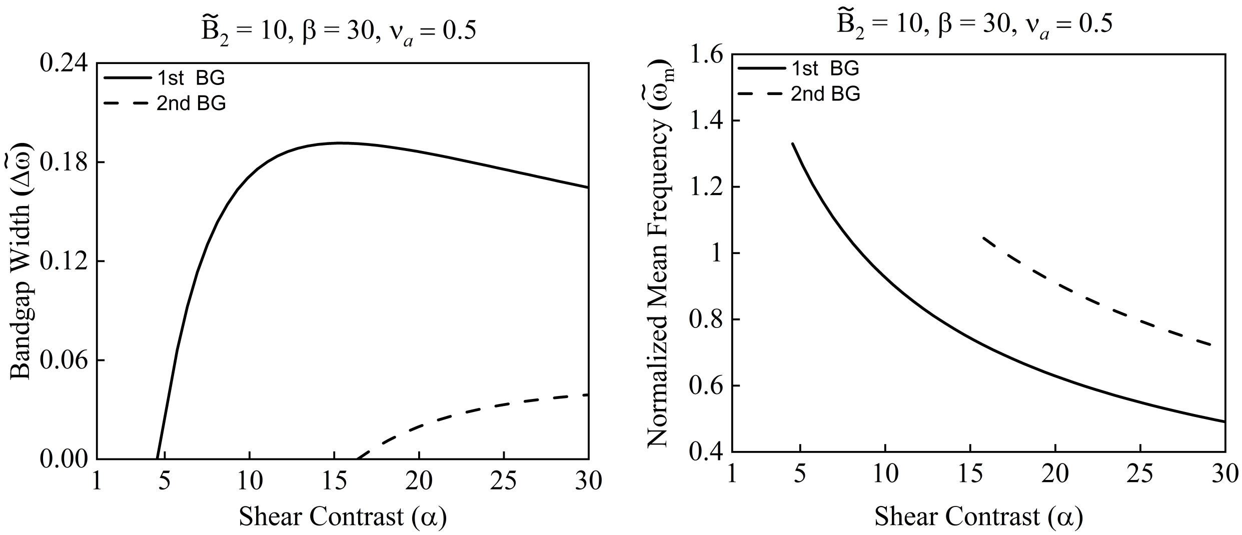

(a) (b)

Figure 6: Variation of the first and second band gap (a) widths, and (b) mean of the frequency limits as a function of shear contrast parameter α.

constants as: $\alpha = 30$, $\beta = 30$, and $\tilde{B}_2 = 10$. The volume fraction $\nu_a = 0$ represents the isotropic homogeneous body made up of phase b only while that of 1 corresponds to body made up of phase a only. Figures 9(a) and 9(b) illustrate the variation of the widths and mean of the frequency limits of first and second bandgaps as a function of volume fraction of the inclusion phase ν_a, respectively. The first bandgap opens at about $\nu_a = 0.25$, and attain a maximum value at $\nu_a = 0.81$, and closes at $\nu_a = 0.93$. The variation of second band gap width also follows the similar trend: band gap opens at $\nu_a = 0.36$ and reaches maximum at $\nu_a = 0.56$, and closes at $\nu_a = 0.64$. It is evident from Fig. 9(a) that the width of the both the band gaps attain maximum value when the concentration of the harder phase a is a bit more than the softer phase b. The maximum value of the first bandgap width is $\Delta\tilde{\omega}\mathrm{max} = 0.4252$, and the corresponding mean of the frequency limits is $\tilde{\omega}\mathrm{m} = 0.7656$. The maximum width of the second bandgap is $\Delta\tilde{\omega}\mathrm{max} = 0.0492$, and the corresponding mean of the frequency limits is $\tilde{\omega}_{\mathrm{m}} = 0.7739$. From Fig. 9(b), it can be observed that the location of the existing band gaps shifts towards higher frequency with an increase in the volume fraction of the harder phases. These trends are similar to the observations reported in the literature (Shmuel, 2013) regarding soft phononic composites.

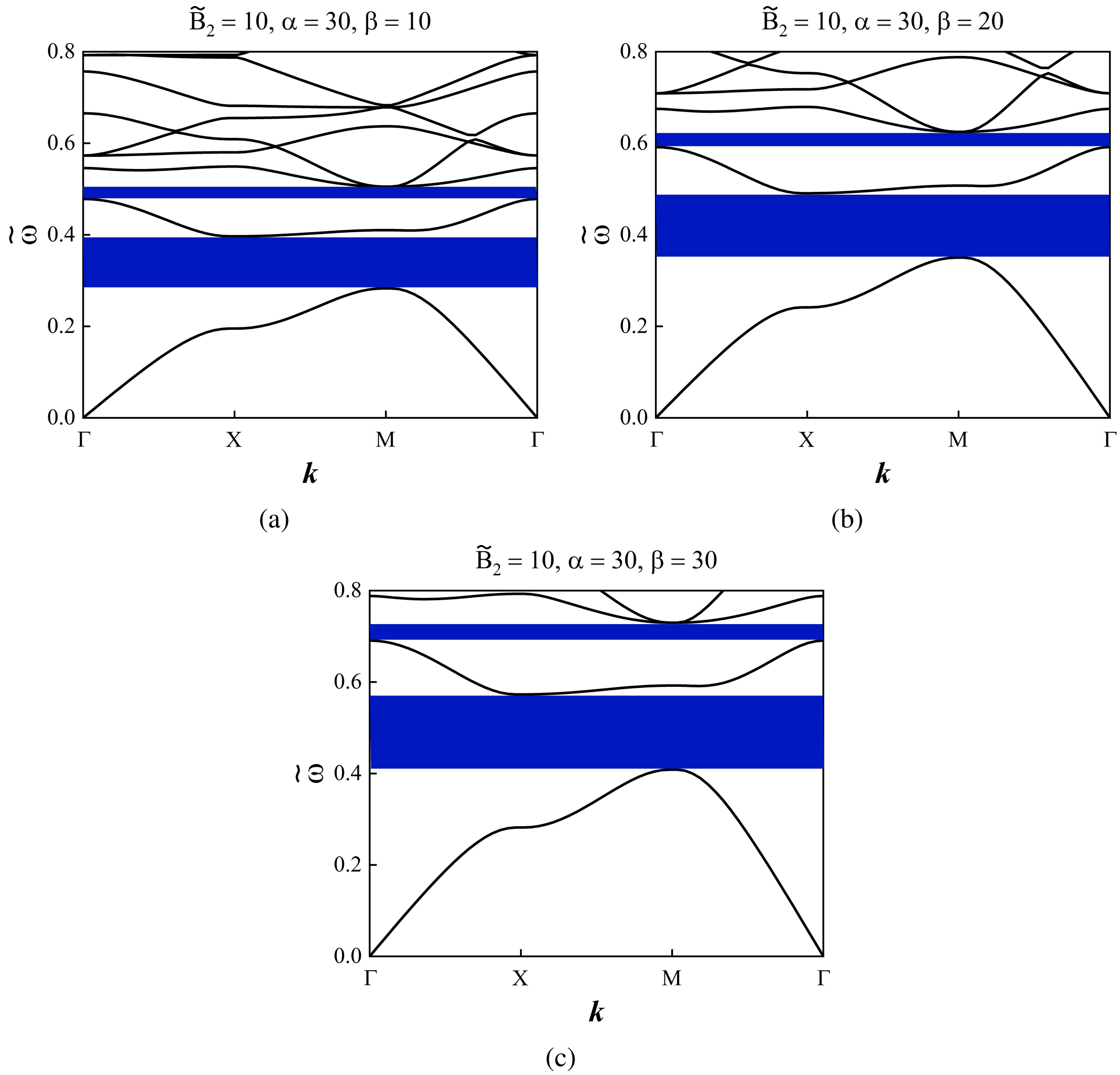

Figure 7: Band structures of the two-phase HMSC at different values of magnetic contrast parameter β, while keeping the shear contrast parameter α, and the normalized magnetic flux density $\tilde{B}_2$ as constant.

5.3. Effect of geometry of inclusion phase

Finally, we investigate the dependence of the anti-plane wave band gap characteristics on geometry of the inclusion phase a. To do so, we consider three configurations of the unit cells as: (I) single central circular inclusion, (II) single central square inclusion, and (III) inclusion at multiple locations) as displayed in top panel of Figs. 10(a-c), respectively. For a one-to-one comparison of the different geometry of the inclusions, we extract the the band gaps for all three cases at same volume fraction $\nu_a = 0.5$ and material parameters: $\alpha = 30$, and $\beta = 10$. The unit cell with circular inclusion is discretized with 1329 four noded quadrilateral elements while the

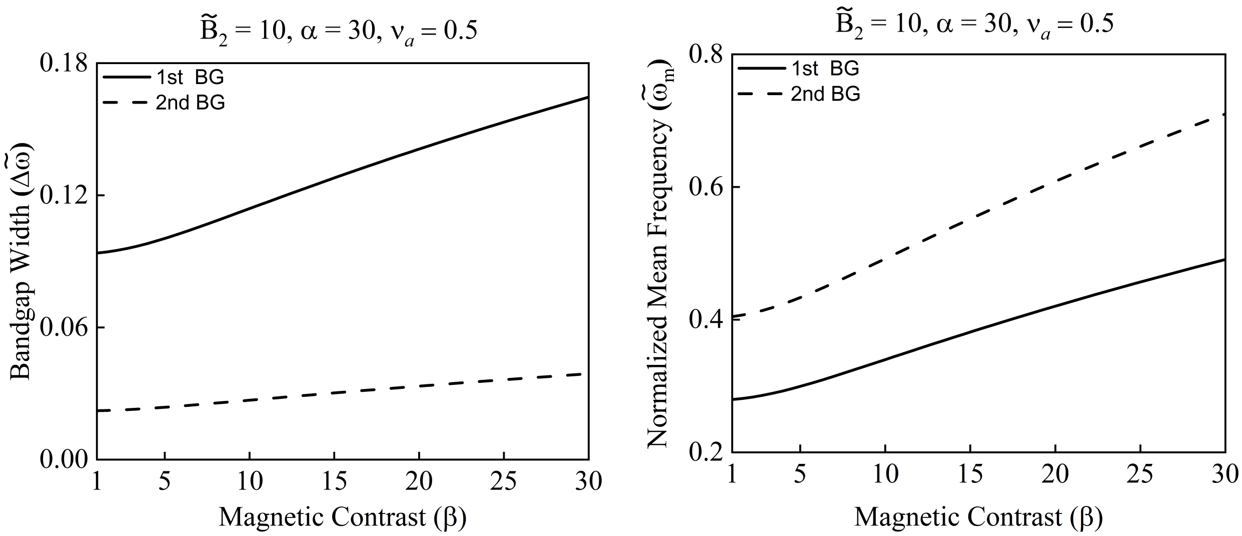

(a) (b)

Figure 8: Variation of the first and second band gap (a) widths, and (b) mean of the frequency limits as a function of magnetic contrast parameter β.

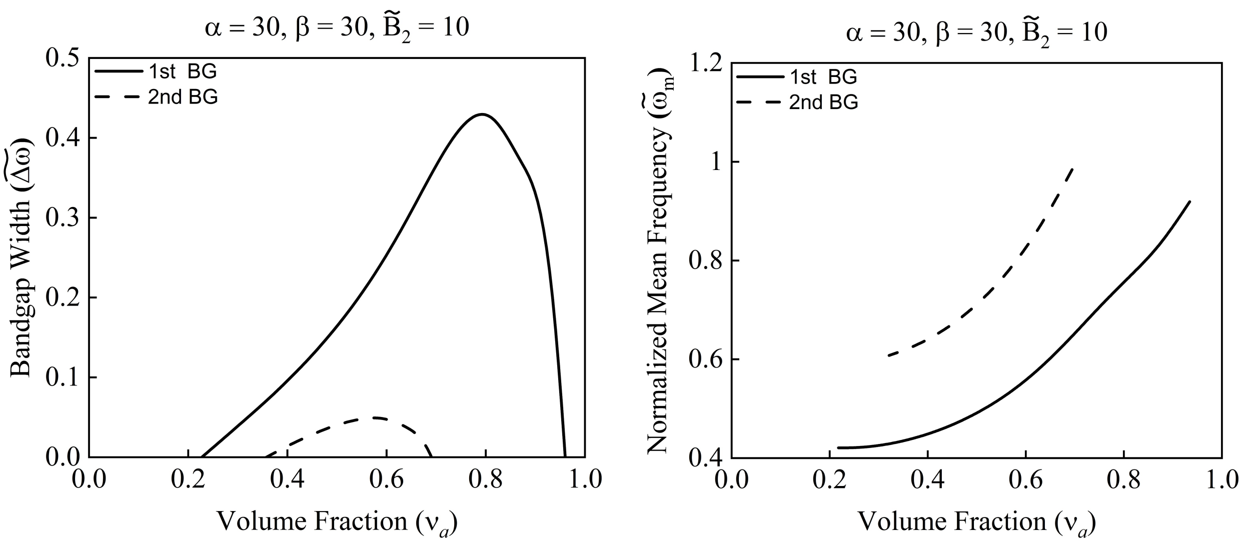

(a) (b)

Figure 9: Variation of the first and second band gap (a) widths, and (b) mean of the frequency limits as a function of the volume fraction of inclusion phase ν_a.

unit cells with square and multiple inclusions are discretized with 1156 four noded quadrilateral elements. Middle panel of Fig. 10 displays the band structures for aforementioned three unit cells, respectively, when the applied normalized magnetic flux density $\tilde{B}_2 = 0$, while that at $\tilde{B}_2 = 10$, are displayed in the bottom panel, respectively. As evident from Fig. 10, for both the values of $\tilde{B}_2$, the unit cell with inclusion at multiple location exhibit the widest first band gap, while the unit cell with circular inclusion exhibit highest second band gap. Further, as expected, the width and the location of the band gaps for all the three cases is bound to be enhanced with the application of applied magnetic flux density. The inferences from this section demonstrate the significant dependence of the band gap widths and their location on the layout or micro-structure of the unit cell. Here, the third layout of the unit cell is obtained by randomly putting inclusions at multiple locations, while other two layouts are the with standard cross-sections of the inclusion. However, an optimized unit cell layout with optimal distribution of phases for wide and tunable band gaps can be obtained using

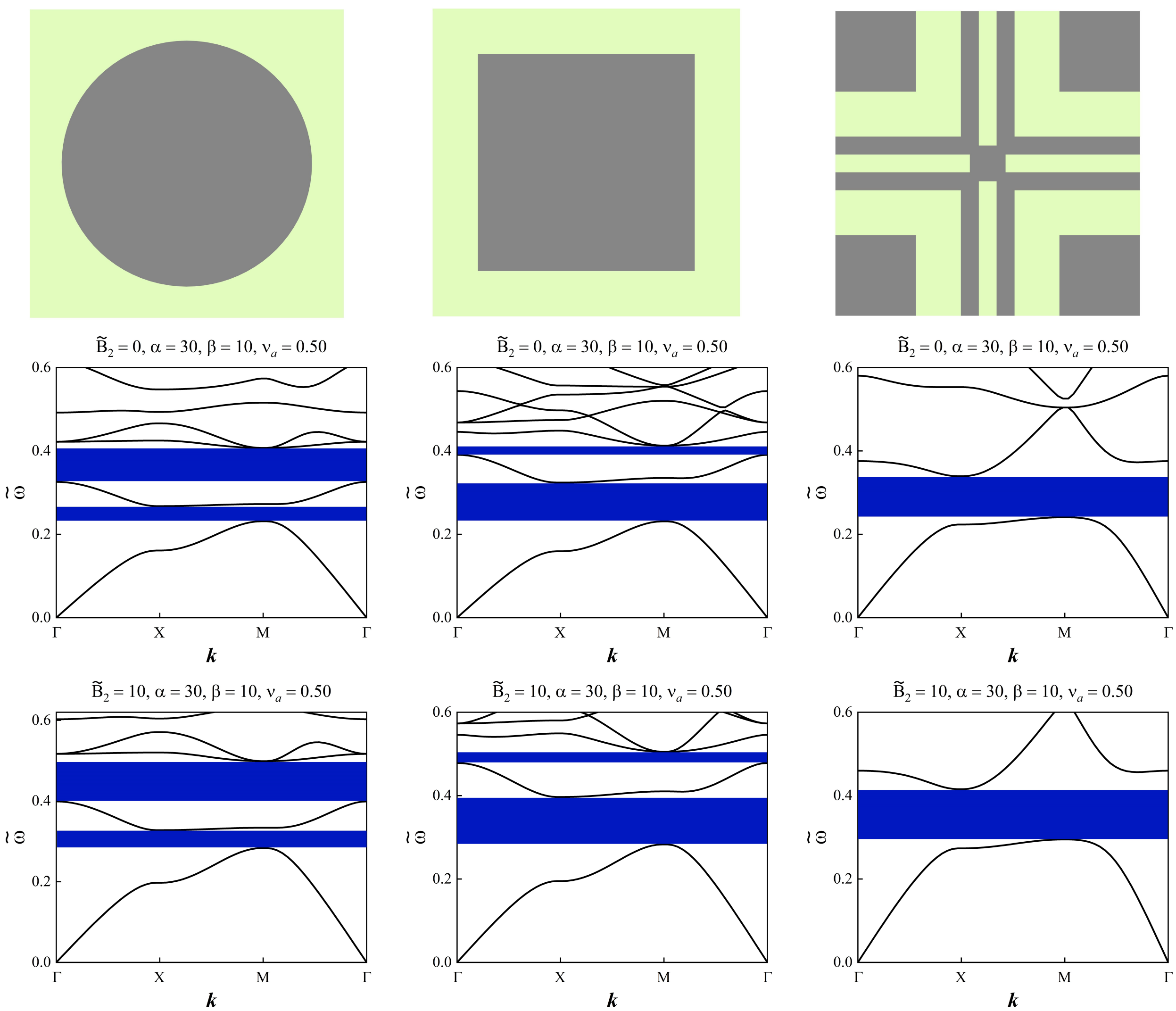

(a) (b) (c)

Figure 10: The layout of the unit cells with (a) single central circular inclusion, (b) single central square inclusion, and (c) inclusion at multiple locations, and corresponding band structures at two different levels of applied magnetic flux density $\tilde{B}_2 = 0$ (middle) and $\tilde{B}_2 = 10$ (bottom).

.

the topology optimization schemes (Bendsoe & Sigmund, 2003; Sigmund & Søndergaard Jensen, 2003) such as genetic algorithm (GA) (Manktelow et al., 2013; Hedayatrasa et al., 2016; Bortot et al., 2018), gradient based optimization schemes (Bacigalupo et al., 2017; Sharma et al., 2022b,a; Dalklint et al., 2022), etc. The finite element framework reported here may be used as a starting point for the topology optimization of HMSCs in future study.

6. Conclusions

In this work, we have presented a theoretical model for extracting the anti-plane wave bandgaps in finitely deformed two-phase 2D periodic HMSCs. Specifically, we implemented the finite element method and the Bloch-Floquet theorem to solve the governing incremental anti-plane wave equations. Through numerical computations of the band structures at various levels of applied magnetic flux density, we characterized the magnetic tunability of anti-plane band gaps in the representative hard-magnetic soft composite materials. At last, we explored the effect of material parameter contrasts and geometry of the inclusion phase on the band gap characteristics. The inferences drawn from the current study are summarized below:

1. We found that the two-phase HMSC under consideration contracts (i.e., experiences lateral stretch with $\lambda > 1$) in the direction of applied normalized magnetic flux density when the magnetic flux is applied in the opposite direction of the residual magnetic flux density. Conversely, we observed expansion (i.e., lateral stretch with $\lambda < 1$) of the composite when residual magnetic flux density aligns with applied magnetic flux density.
2. It has been observed that magnetic loading has a positive impact on the characteristics of the bandgap. When the magnitude of the applied magnetic flux density increases, the bandgap widens and shifts towards higher frequencies. However, the rate at which the bandgap width increases is greater when the applied magnetic flux density aligns with the direction of the residual magnetic flux density.
3. In the context of material parameter contrasts, the shear contrast parameter α has the most significant effect on the band gap size. The influence of the magnetic parameter contrast β was found to be more moderate for the range of contrast values examined in this study. An increase in the shear contrast parameter α shifts the band gaps towards the lower frequency

range, while in contrast, an increase in the magnetic contrast parameter β shifts the band gap location towards a higher frequency range.

4. Opening, closing, size and the location of the anti-plane wave band gaps exhibit a significant dependence on the volume fraction of the constituent phases in the HMSC. Specifically, the first bandgap width is maximized when the volume fraction, ν_a, is 0.81, while the second bandgap width is maximized when ν_a is 0.56.
5. We have demonstrated a notable dependence of the band gap widths and their location on the layout or micro-structure of the unit cell. Among the three considered layouts of the unit cells, the unit cell with inclusions at multiple locations exhibits the highest band gap width, given the specified material parameters.

The results obtained in this study could serve as robust theoretical guidance for designing and manufacturing of magnetically tunable hard-magnetic soft wave devices, as well as for wave-based characterization techniques of HMSMs. The finite element framework presented in this work establishes an initial foundation for future research on designing and developing wide and tunable band gaps in HMSCs through topology optimization. Although our current focus has been on anti-plane wave band gaps, exploring the tunability of in-plane wave band gaps in two-phase HMSCs could be an immediate area of interest for further investigation.

Acknowledgment

The authors would like to express their gratitude to IIT Jodhpur for their financial support through institute initial research Grant No. I/SEED/ATS/20220087.

References

Alam, Z., Padmanabhan, S., & Sharma, A. K. (2023). Magnetically tunable longitudinal wave band gaps in hard-magnetic soft laminates. *International Journal of Mechanical Sciences*, *249*, 108262. doi:10.1016/j.ijmecsci.2023.108262.

Alam, Z., & Sharma, A. (2022). Functionally graded soft dielectric elastomer phononic crystals: Finite deformation, electro-elastic longitudinal waves, and band gaps tunability via electro-mechanical loading. *International Journal of Applied Mechanics*, *14*. doi:10.1142/S1758825122500508.

Bacigalupo, A., Gnecco, G., Lepidi, M., & Gambarotta, L. (2017). Optimal design of low-frequency band gaps in anti-tetrachiral lattice meta-materials. *Composites Part B: Engineering*, *115*, 341–59. doi:https://doi.org/10.1016/j.compositesb.2016.09.062. Composite lattices and multiscale innovative materials and structures.

Badreddine Assouar, M., Senesi, M., Oudich, M., Ruzzene, M., & Hou, Z. (2012). Broadband plate-type acoustic metamaterial for low-frequency sound attenuation. *Applied Physics Letters*, *101*. doi:10.1063/1.4764072.

Bendsoe, M. P., & Sigmund, O. (2003). *Topology optimization: theory, methods, and applications*. Springer Science & Business Media. doi:https://doi.org/10.1007/978-3-662-05086-6.

Bertoldi, K., & Boyce, M. C. (2008). Mechanically triggered transformations of phononic band gaps in periodic elastomeric structures. *Phys. Rev. B*, *77*, 052105. URL: https://link.aps.org/doi/10.1103/PhysRevB.77.052105. doi:10.1103/PhysRevB.77.052105.

Bortot, E., Amir, O., & Shmuel, G. (2018). Topology optimization of dielectric elastomers for wide tunable band gaps. *International Journal of Solids and Structures*, *143*, 262–73. doi:https://doi.org/10.1016/j.ijsolstr.2018.03.014.

Bou Matar, O., Robillard, J. F., Vasseur, J. O., Hladky-Hennion, A.-C., Deymier, P. A., Pernod, P., & Preobrazhensky, V. (2012). Band gap tunability of magneto-elastic phononic crystal. *Journal of Applied Physics*, *111*. URL: https://doi.org/10.1063/1.3687928. doi:10.1063/1.3687928. 054901.

Chen, Y., Wu, B., Destrade, M., & Chen, W. (2022). Voltage-controlled topological interface states for bending waves in soft dielectric phononic crystal plates. *International Journal of Solids and Structures*, *259*, 112013. doi:https://doi.org/10.1016/j.ijsolstr.2022.112013.

Chen, Y., Wu, B., Su, Y., & Chen, W. (2019). Tunable Two-Way Unidirectional Acoustic Diodes: Design and Simulation. *Journal of Applied Mechanics*, *86*. doi:10.1115/1.4042321. 031010.

Dalklint, A., Wallin, M., Bertoldi, K., & Tortorelli, D. (2022). Tunable phononic bandgap materials designed via topology optimization. *Journal of the Mechanics and Physics of Solids*, *163*, 104849. doi:https://doi.org/10.1016/j.jmps.2022.104849.

Dorfmann, L., & Ogden, R. W. (2014). *Nonlinear theory of electroelastic and magnetoelastic interactions* volume 1. Springer. doi:10.1007/978-1-4614-9596-3.

Dubus, B., Croënne, C., Hladky-Hennion, A.-C., Vasseur, J., Tinel, A., & Morvan, B. (2011). Development of elastic super-lenses made of phononic crystals for ultrasonic imaging. (p. 989 – 990).

Felippa, C. (2001). Introduction to finite element methods. multifreedom constraints ii (lecture notes).

Garcia-Gonzalez, D., Moreno, M., Valencia, L., Arias, A., & Velasco, D. (2021). Influence of elastomeric matrix and particle volume fraction on the mechanical response of magneto-active polymers. *Composites Part B: Engineering*, *215*, 108796. doi:https://doi.org/10.1016/j.compositesb.2021.108796.

Gei, M., Roccabianca, S., & Bacca, M. (2011). Controlling bandgap in electroactive polymer-based structures. *IEEE/ASME Transactions on Mechatronics*, *16*, 102–7. doi:10.1109/TMECH.2010.2090165.

Gent, A. N. (1996). A new constitutive relation for rubber. *Rubber Chemistry and Technology*, *69*, 59–61. doi:10.5254/1.3538357.

Getz, R., Kochmann, D. M., & Shmuel, G. (2017). Voltage-controlled complete stopbands in two-dimensional soft dielectrics. *International Journal of Solids and Structures*, *113-114*, 24–36. doi:https://doi.org/10.1016/j.ijsolstr.2016.10.002.

Gharibi, H., & Mehaney, A. (2021). Two-dimensional phononic crystal sensor for volumetric detection of hydrogen peroxide (h2o2) in liquids. *Physica E: Low-Dimensional Systems and Nanostructures*, *126*. doi:10.1016/j.physe.2020.114429.

Hedayatrasa, S., Abhary, K., Uddin, M., & Guest, J. K. (2016). Optimal design of tunable phononic bandgap plates under equibiaxial stretch. *Smart Materials and Structures*, *25*. doi:10.1088/0964-1726/25/5/055025.

Hu, Q., Yang, W., & Zhang, S. (2022). Studies on band structure of magneto-elastic phononic crystal nanoplates using the nonlocal theory. *Physics Letters A*, *423*, 127820. doi:https://doi.org/10.1016/j.physleta.2021.127820.

Jandron, M., & Henann, D. L. (2018). A numerical simulation capability for electroelastic wave propagation in dielectric elastomer composites: Application to tunable soft phononic crystals. *International Journal of Solids and Structures*, *150*, 1–21. doi:10.1016/j.ijsolstr.2018.04.023.

Karami Mohammadi, N., Galich, P. I., Krushynska, A. O., & Rudykh, S. (2019). Soft Magnetoactive Laminates: Large Deformations, Transverse Elastic Waves and Band Gaps Tunability by a Magnetic Field. *Journal of Applied Mechanics*, *86*. doi:10.1115/1.4044497. 111001.

Khelif, A., Choujaa, A., Benchabane, S., Djafari-Rouhani, B., & Laude, V. (2004). Guiding and bending of acoustic waves in highly confined phononic crystal waveguides. *Applied Physics Letters*, *84*, 4400 – 4402. doi:10.1063/1.1757642.

Kim, E., & Yang, J. (2014). Wave propagation in single column woodpile phononic crystals: Formation of tunable band gaps. *Journal of the Mechanics and Physics of Solids*, *71*, 33–45. doi:https://doi.org/10.1016/j.jmps.2014.06.012.

Kim, Y., Parada, G., Liu, S., & Zhao, X. (2019). Ferromagnetic soft continuum robots. *Science Robotics*, *4*. doi:10.1126/SCIROBOTICS.AAX7329.

Kim, Y., Yuk, H., Zhao, R., Chester, S. A., & Zhao, X. (2018). Printing ferromagnetic domains for untethered fast-transforming soft materials. *Nature*, *558*, 274–9. doi:10.1038/s41586-018-0185-0.

Kittel, C., McEuen, P., & McEuen, P. (1996). *Introduction to solid state physics* volume 8. Wiley New York.

Kushwaha, M. S., Halevi, P., Dobrzynski, L., & Djafari-Rouhani, B. (1993). Acoustic band structure of periodic elastic composites. *Physical review letters*, *71*, 2022. doi:10.1103/PhysRevLett.71.2022.

Kushwaha, M. S., Halevi, P., Martinez, G., Dobrzynski, L., & Djafari-Rouhani, B. (1994). Theory of acoustic band structure of periodic elastic composites. *Physical Review B*, *49*, 2313. doi:10.1103/PhysRevB.49.2313.

Lee, M., Park, T., Kim, C., & Park, S.-M. (2020). Characterization of a magneto-active membrane actuator comprising hard magnetic particles with varying crosslinking degrees. *Materials & Design*, *195*, 108921. doi:https://doi.org/10.1016/j.matdes.2020.108921.

Li, B., Yan, W., & Gao, Y. (2022). Tunability of band gaps of programmable hard-magnetic soft material phononic crystals. *Acta Mechanica Solida Sinica*, *35*, 719–32. doi:10.1007/s10338-022-00336-1.

Liu, X., Chen, N., Jiao, J., & Liu, J. (2023). Pneumatic soft phononic crystals with tunable band gap. *International Journal of Mechanical Sciences*, *240*, 107906. doi:https://doi.org/10.1016/j.ijmecsci.2022.107906.

Lucarini, S., Hossain, M., & Garcia-Gonzalez, D. (2022). Recent advances in hard-magnetic soft composites: Synthesis, characterisation, computational modelling, and applications. *Composite Structures*, *279*, 114800. doi:https://doi.org/10.1016/j.compstruct.2021.114800.

Lum, G. Z., Ye, Z., Dong, X., Marvi, H., Erin, O., Hu, W., & Sitti, M. (2016). Shape-programmable magnetic soft matter. *Proceedings of the National Academy of Sciences*, *113*, E6007–15. doi:10.1073/pnas.1608193113.

Manktelow, K. L., Leamy, M. J., & Ruzzene, M. (2013). Topology design and optimization of nonlinear periodic materials. *Journal of the Mechanics and Physics of Solids*, *61*, 2433–53. doi:https://doi.org/10.1016/j.jmps.2013.07.009.

Moradi, P., & Bahrami, A. (2019). Three channel ghz-ranged demultiplexer in solid-solid phononic crystals. *Chinese Journal of Physics*, *59*, 291 – 297. doi:10.1016/j.cjph.2019.03.005.

Moreno-Mateos, M. A., Hossain, M., Steinmann, P., & Garcia-Gonzalez, D. (2023). Hard magnetics in ultra-soft magnetorheological elastomers enhance fracture toughness and delay crack propagation. *Journal of the Mechanics and Physics of Solids*, *173*, 105232. doi:https://doi.org/10.1016/j.jmps.2023.105232.

Nagal, N., Srivastava, S., Pandey, C., Gupta, A., & Sharma, A. K. (2022). Alleviation of residual vibrations in hard-magnetic soft actuators using a command-shaping scheme. *Polymers*, *14*. doi:10.3390/polym14153037.

Nandan, S., Sharma, D., & Sharma, A. K. (2023). Viscoelastic Effects on the Nonlinear Oscillations of Hard-Magnetic Soft Actuators. *Journal of Applied Mechanics*, *90*. doi:10.1115/1.4056816. 061001.

Nimmagadda, C., & Matlack, K. H. (2019). Thermally tunable band gaps in architected metamaterial structures. *Journal of Sound and Vibration*, *439*, 29–42. doi:https://doi.org/10.1016/j.jsv.2018.09.053.

Pierce, C. D., Willey, C. L., Chen, V. W., Hardin, J. O., Berrigan, J. D., Juhl, A. T., & Matlack, K. H. (2020). Adaptive elastic metastructures from magneto-active elastomers. *Smart Materials and Structures*, *29*. doi:10.1088/1361-665X/ab80e4.

Raghavan, L., & Phani, A. S. (2013). Local resonance bandgaps in periodic media: Theory and experiment. *The Journal of the Acoustical Society of America*, *134*, 1950–9. doi:10.1121/1.4817894.

Rahmati, A. H., Jia, R., Tan, K., Liu, L., Zhao, X., Deng, Q., & Sharma, P. (2023a). Giant magnetoelectricity in soft materials using hard magnetic soft materials. *Materials Today Physics*, *31*, 100969. doi:https://doi.org/10.1016/j.mtphys.2023.100969.

Rahmati, A. H., Jia, R., Tan, K., Zhao, X., Deng, Q., Liu, L., & Sharma, P. (2023b). Theory of hard magnetic soft materials to create magnetoelectricity. *Journal of the Mechanics and Physics of Solids*, *171*, 105136. doi:https://doi.org/10.1016/j.jmps.2022.105136.

Rudykh, S., & Boyce, M. C. (2014). Transforming wave propagation in layered media via instability-induced interfacial wrinkling. *Phys. Rev. Lett.*, *112*, 034301. URL: https://link.aps.org/doi/10.1103/PhysRevLett.112.034301. doi:10.1103/PhysRevLett.112.034301.

Sano, T. G., Pezzulla, M., & Reis, P. M. (2022). A kirchhoff-like theory for hard magnetic rods under geometrically nonlinear deformation in three dimensions. *Journal of the Mechanics and Physics of Solids*, *160*, 104739. doi:https://doi.org/10.1016/j.jmps.2021.104739.

Sharma, A. K., Joglekar, M., Joglekar, D., & Alam, Z. (2022a). Topology optimization of soft compressible phononic laminates for widening the mechanically tunable band gaps. *Composite Structures*, *289*, 115389. doi:https://doi.org/10.1016/j.compstruct.2022.115389.

Sharma, A. K., Kosta, M., Shmuel, G., & Amir, O. (2022b). Gradient-based topology optimization of soft dielectrics as tunable phononic crystals. *Composite Structures*, *280*, 114846. doi:https://doi.org/10.1016/j.compstruct.2021.114846.

Shim, J., Wang, P., & Bertoldi, K. (2015). Harnessing instability-induced pattern transformation to design tunable phononic crystals. *International Journal of Solids and Structures*, *58*, 52–61. doi:https://doi.org/10.1016/j.ijsolstr.2014.12.018.

Shmuel, G. (2013). Electrostatically tunable band gaps in finitely extensible dielectric elastomer fiber composites. *International Journal of Solids and Structures*, *50*, 680–6. doi:https://doi.org/10.1016/j.ijsolstr.2012.10.028.

Shmuel, G., & Band, R. (2016). Universality of the frequency spectrum of laminates. *Journal of the Mechanics and Physics of Solids*, *92*, 127–36. doi:https://doi.org/10.1016/j.jmps.2016.04.001.

Shmuel, G., & deBotton, G. (2012). Band-gaps in electrostatically controlled dielectric laminates subjected to incremental shear motions. *Journal of the Mechanics and Physics of Solids*, *60*, 1970–81. doi:https://doi.org/10.1016/j.jmps.2012.05.006.

Sigalas, M., & Economou, E. (1992). Elastic and acoustic wave band structure. *Journal of Sound and Vibration*, *158*, 377–82. doi:https://doi.org/10.1016/0022-460X(92)90059-7.

Sigmund, O., & Søndergaard Jensen, J. (2003). Systematic design of phononic band–gap materials and structures by topology optimization. *Philosophical Transactions of the Royal Society of London. Series A: Mathematical, Physical and Engineering Sciences*, *361*, 1001–19. doi:10.1098/rsta.2003.1177.

Vasileiadis, T., Varghese, J., Babacic, V., Gomis-Bresco, J., Navarro Urrios, D., & Graczykowski, B. (2021). Progress and perspectives on phononic crystals. *Journal of Applied Physics*, *129*. doi:10.1063/5.0042337.

Vatanabe, S. L., Paulino, G. H., & Silva, E. C. (2014). Maximizing phononic band gaps in piezocomposite materials by means of topology optimization. *The Journal of the Acoustical Society of America*, *136*, 494–501. doi:10.1121/1.4887456.

Wang, L., & Bertoldi, K. (2012). Mechanically tunable phononic band gaps in three-dimensional periodic elastomeric structures. *International Journal of Solids and Structures*, *49*, 2881–5. doi:https://doi.org/10.1016/j.ijsolstr.2012.05.008. Proceedings of International Union of Theoretical and Applied Mechanics Symposium.

Wang, L., Kim, Y., Guo, C. F., & Zhao, X. (2020). Hard-magnetic elastica. *Journal of the Mechanics and Physics of Solids*, *142*, 104045. doi:https://doi.org/10.1016/j.jmps.2020.104045.

Wang, L., Zheng, D., Harker, P., Patel, A. B., Guo, C. F., & Zhao, X. (2021). Evolutionary design of magnetic soft continuum robots. *Proceedings of the National Academy of Sciences of the United States of America*, *118*. doi:10.1073/pnas.2021922118.

Wang, Y.-Z., Li, F.-M., Huang, W.-H., Jiang, X., Wang, Y.-S., & Kishimoto, K. (2008). Wave band gaps in two-dimensional piezoelectric/piezomagnetic phononic crystals. *International Journal of Solids and Structures*, *45*, 4203 – 4210. doi:10.1016/j.ijsolstr.2008.03.001.

Wang, Y.-Z., Li, F.-M., Huang, W.-H., & Wang, Y.-S. (2007). Effects of inclusion shapes on the band gaps in two-dimensional piezoelectric phononic crystals. *Journal of Physics: Condensed Matter*, *19*, 496204. doi:10.1088/0953-8984/19/49/496204.

Wang, Y.-Z., Li, F.-M., Kishimoto, K., Wang, Y.-S., & Huang, W.-H. (2010). Band gaps of elastic waves in three-dimensional piezoelectric phononic crystals with initial stress. *European Journal of Mechanics, A/Solids*, *29*, 182–9. doi:10.1016/j.euromechsol.2009.09.005.

Wu, S., Hamel, C. M., Ze, Q., Yang, F., Qi, H. J., & Zhao, R. (2020a). Evolutionary algorithm-guided voxel-encoding printing of functional hard-magnetic soft active materials. *Advanced Intelligent Systems*, *2*, 2000060. doi:https://doi.org/10.1002/aisy.202000060.

Wu, S., Hu, W., Ze, Q., Sitti, M., & Zhao, R. (2020b). Multifunctional magnetic soft composites: A review. *Multifunctional materials*, *3*, 042003. doi:10.1088/2399-7532/abcb0c.

Xia, B., Chen, N., Xie, L., Qin, Y., & Yu, D. (2016). Temperature-controlled tunable acoustic metamaterial with active band gap and negative bulk modulus. *Applied Acoustics*, *112*, 1–9. doi:https://doi.org/10.1016/j.apacoust.2016.05.005.

Xia, B., Wang, G., & Zheng, S. (2019). Robust edge states of planar phononic crystals beyond high-symmetry points of brillouin zones. *Journal of the Mechanics and Physics of Solids*, *124*, 471–88. doi:https://doi.org/10.1016/j.jmps.2018.11.001.

Yan, D., Aymon, B. F., & Reis, P. M. (2023). A reduced-order, rotation-based model for thin hard-magnetic plates. *Journal of the Mechanics and Physics of Solids*, *170*, 105095. doi:https://doi.org/10.1016/j.jmps.2022.105095.

Zhang, G., & Gao, X.-L. (2020). Band gaps for wave propagation in 2-d periodic three-phase composites with coated star-shaped inclusions and an orthotropic matrix. *Composites Part B: Engineering*, *182*, 107319. doi:https://doi.org/10.1016/j.compositesb.2019.107319.

Zhang, P., & To, A. C. (2013). Broadband wave filtering of bioinspired hierarchical phononic crystal. *Applied Physics Letters*, *102*. doi:10.1063/1.4799171.

Zhang, Q., Cherkasov, A. V., Arora, N., Hu, G., & Rudykh, S. (2023). Magnetic field-induced asymmetric mechanical metamaterials. *Extreme Mechanics Letters*, *59*, 101957. doi:https://doi.org/10.1016/j.eml.2023.101957.

Zhang, Q., & Rudykh, S. (2022). Magneto-deformation and transverse elastic waves in hard-magnetic soft laminates. *Mechanics of Materials*, *169*, 104325. doi:j.mechmat.2022.104325.

Zhao, R., Kim, Y., Chester, S. A., Sharma, P., & Zhao, X. (2019). Mechanics of hard-magnetic soft materials. *Journal of the Mechanics and Physics of Solids*, *124*, 244–63. doi:https://doi.org/10.1016/j.jmps.2018.10.008.

Zhao, Z., Chen, Y., Hu, X., Bao, R., Wu, B., & Chen, W. (2023). Vibrations and waves in soft dielectric elastomer structures. *International Journal of Mechanical Sciences*, *239*, 107885. doi:https://doi.org/10.1016/j.ijmecsci.2022.107885.

Zhao, Z., & Zhang, X. S. (2022). Topology optimization of hard-magnetic soft materials. *Journal of the Mechanics and Physics of Solids*, *158*, 104628. doi:https://doi.org/10.1016/j.jmps.2021.104628.

Zheng, L.-Y., Wu, Y., Ni, X., Chen, Z.-G., Lu, M.-H., & Chen, Y.-F. (2014). Acoustic cloaking by a near-zero-index phononic crystal. *Applied Physics Letters*, *104*. doi:10.1063/1.4873354.